Spring 2021

Atmospheric Corrosion of Galvanically Coupled Aluminum Alloys and Carbon Steel

Mitchell Felde

Atmospheric Corrosion of Galvanically Coupled Aluminum Alloys and Carbon Steel

Honors Research Project

4250 497-003

April 28th, 2021

Author

Mitchell Felde

Faculty Advisor

Dr. David M. Bastidas

Co-Advisor

Juan Bosch

Table of Contents

Executive Summary

Aluminum alloys are a steadily growing material being commonly used in lieu of typical steels. Additional alloying, heat treatment, and other property enhancing processes are expanding the use of these alloys. However, with this expansion, galvanic corrosion is becoming more of an issue in the design stage due to the combination of these alloys with steels. The automotive industry is one industry where the use of aluminum alloys is becoming common practice. Aluminum alloys provide a lightweight aspect over the conventional carbon steel that was used previously. As a result of this transition towards more lightweight materials, galvanic coupling is becoming a major issue in the automotive industry. A key understanding of the mechanism and kinetics is required in order to continue this transition to lightweight materials safely and economically. This issue can be better understood with the results of this project and provide better guidance for those in industry.

For this study, three materials were investigated individually and coupled in two solutions. The materials were carbon steel 1018, aluminum alloy (AA) 6111, and AA 6022. The investigated solutions were 0.6M NaCl and 0.06M NaCl. To simulate the effects of atmospheric environments, rotating disk electrode setup was used while performing cyclic potentiodynamic polarization (CPP) and electrochemical impedance spectroscopy (EIS) at increasing rotation speeds. The investigated speeds were 0, 100, 500, 1000, and 2000 rpm. Scanning Kelvin Probe (SKP) was performed to characterize the surface potential gradient resultant from the galvanic coupling. The measured galvanic current between the CS1018 and AA6111 was measured to be 6.794 $\mu A/cm^2$ and 0.354 $\mu A/cm^2$ in 0.6M NaCl and 0.06M NaCl respectively. The measured galvanic current between the CS1018 and AA6022 was measured to be 2.815 $\mu A/cm^2$ and 0.018 $\mu A/cm^2$ in 0.6M NaCl and 0.06M NaCl respectively. These measured currents indicate that the aluminum is undergoing accelerated corrosion as a result of the galvanic couple. This basis in conjunction with the results from other characterization methods and experiments provide sufficient reinforcement to this conclusion. For further quantitative results, refer to the **Data and Analysis** section of the report.

Overall, the corrosion behavior of AA6022 demonstrated to perform better than the AA6111 in both 0.6M NaCl and 0.06M NaCl solutions. It demonstrated a lower i_{corr} and more negative E_{corr}. The measured corrosion potential was close to that of the CS1018 in both solutions respectively. This will demonstrate there is a smaller magnitude galvanic coupling effect of AA6022 when coupled with CS1018 in comparison with the AA6111 coupled with CS1018.

As a result of this project, some of the broader implications included acquiring technical skills regarding lab work and data analysis as well as some career skills. Proper sample preparation was required to execute the experiments correctly and ensure the collected data was accurate. Becoming familiar with the computer software used for the potentiostat was another critical skill that furthered my understanding of the scientific implications from the experiments. The career skills that were gained from this project included project planning, advanced time management, and creativity. Outside of the technical aspect, improvements in independence and critical thinking were gained as a result from the project.

Future work for this project includes further studies on other galvanically coupled alloys and developing a mathematical model of the corrosion mechanism in order to allow the prediction of these galvanic couples under different conditions using COMSOL Multiphysics. This will allow the service lifetime establishment and thus, promote the use of these alloys that have certainly improve the fuel efficiency and greenhouse emissions of the automotive industry. Further studies should be performed on other aluminum alloys in order to better optimize the observed reduction in galvanic coupling effect between carbon steel and the alloy. An aluminum alloy which demonstrates no detriments when coupled with carbon steel is desirable. In addition, automotive manufacturers may need to use other alloys to meet certain mechanical specifications outside of those studied in this project. By continuing this research, the manufacturer and society will only benefit from acquiring this knowledge.

Introduction

Aluminum alloys are a steadily growing material being commonly used in the automotive industry. There are many benefits from using aluminum alloys. Weight reduction is a major benefit as it will enhance fuel economy and efficiency of the combustion engine. In turn this will reduce the magnitude of energy required to power the vehicles, decreasing emissions. In addition, aluminum alloys provide much higher corrosion resistance than conventional steels due to a naturally forming alumina (Al_2O_3) film on the material. The thin alumina layer is stable in air and neutral (pH 4-8.5) aqueous solutions [1] [2] [3].

A common issue that industry is encountering with aluminum alloy and carbon steel combinations in design is the galvanic coupling of dissimilar metals. When two dissimilar metals are electrically connected together in the presence of an electrolyte, the metal that is more active will preferentially corrode while the other will not undergo the anodic dissolution. The more active metal, or anode, will undergo anodic dissolution and result in a severe reduction of the lifetime expectancy that may lead to a sudden mechanical failure. Several factors influence the kinetics of this process, some of which include; electrolyte solution, surface roughness, galvanically coupled materials, and area of the dissimilar metals. The electrolyte solution may present itself in various forms from conventional types. Atmospheric conditions must be investigated due to similarities to service use [2].

Experimentation must be performed in order to understand the magnitude and mechanisms surrounding the galvanic coupling of materials. With correct preventative measures, the detrimental effects of galvanic coupling can be correctly mitigated. These mitigation strategies will lead to an increased service life of the materials and greatly increase the safety of the automotive industry.

Background

When two dissimilar metals are electrically connected, or coupled, together in an environment that allows for the flow of ions and electrons, a galvanic corrosion cell will be created. Oxidation reactions occur at the more active metal, or the anode, while reduction reactions occur at the more noble metal, or the cathode. An example of a galvanic cell can be seen below in **Figure 1**.

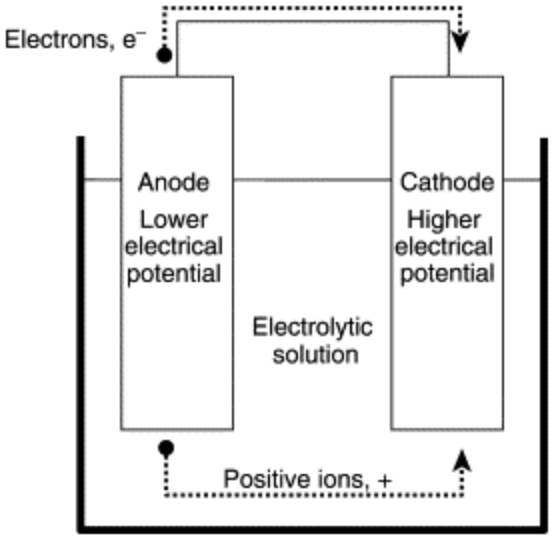

Figure 1. Example of a galvanic cell [4].

The electrochemical reaction occurring at the anode typically consists of the metal oxidizing, $M \rightarrow M^{+}$, which results in the dissolution of the anode. On the other portion, the cathode will involve reduction reactions. These reactions are typically either hydrogen evolution reaction ($2H^{+} + 2e^{-} \rightarrow H_2$) or oxygen reduction reaction ($O_2 + 2H_2O + 4e^{-} \rightarrow 4OH^{-}$). However, when the cathode and anode are coupled, the anode will preferentially corrode. The standard reduction potential of materials in seawater provides useful insight into how such materials may behave when coupled. In **Figure 2**, increasing standard reduction potential is typically associated with materials that will behave as anodes in electrochemical cells while more electropositive materials will behave as cathodes. Based upon this table, aluminum alloys have a more negative standard reduction potential than most steels, demonstrating that aluminum alloys will behave as the anode when coupled with steels.

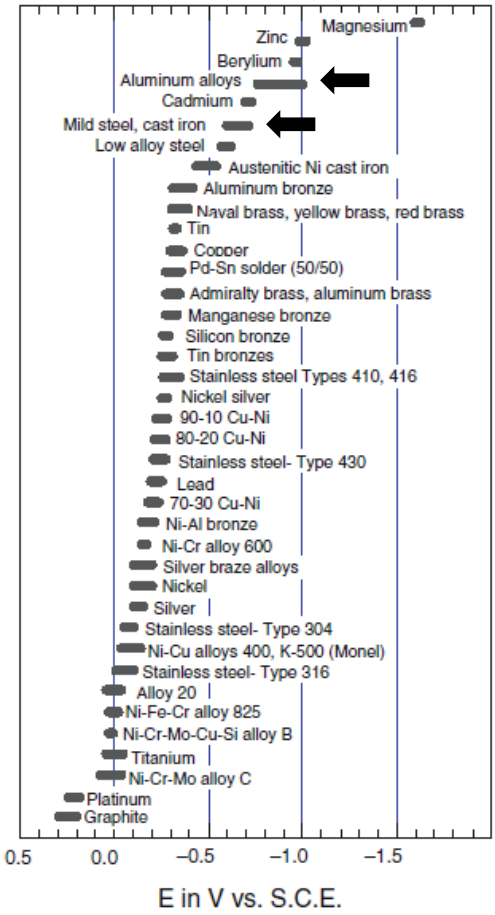

Figure 2. Galvanic Series in Seawater [5].

When adjusting the area of the cathode or anode, a change in the current density of the anode will occur. Increasing the cathode's exposed surface area to the electrolyte solution will result in an increase in the anode's current density. Increasing the anode's exposed surface area to the electrolyte solution while retaining the same area for the cathode will result in a decrease in the anode's corrosion current density. This relationship can be mathematically related through the following relationship, with the assumption that the material is under activation control: [2] [5] [6]

$$i_a = \left(\frac{A_c}{A_a}\right) * i_c \qquad (1)$$

To characterize and understand the corrosion behavior of metals, electrochemical tests must be performed. Cyclic potentiodynamic polarization (CPP) is one such test that applies a polarizing current to the investigated

material, or working electrode, to control the potential. The potential of the working electrode can be controlled to make the material behave anodically or cathodically. CPP tests can be performed to obtain a polarization curve and can be completed by constructing an electrochemical cell that includes a working electrode, a reference electrode, and a counter electrode in a conductive solution connected to a potentiostat. The sample is then polarized above and below its open circuit potential over a specified potential range. [2]

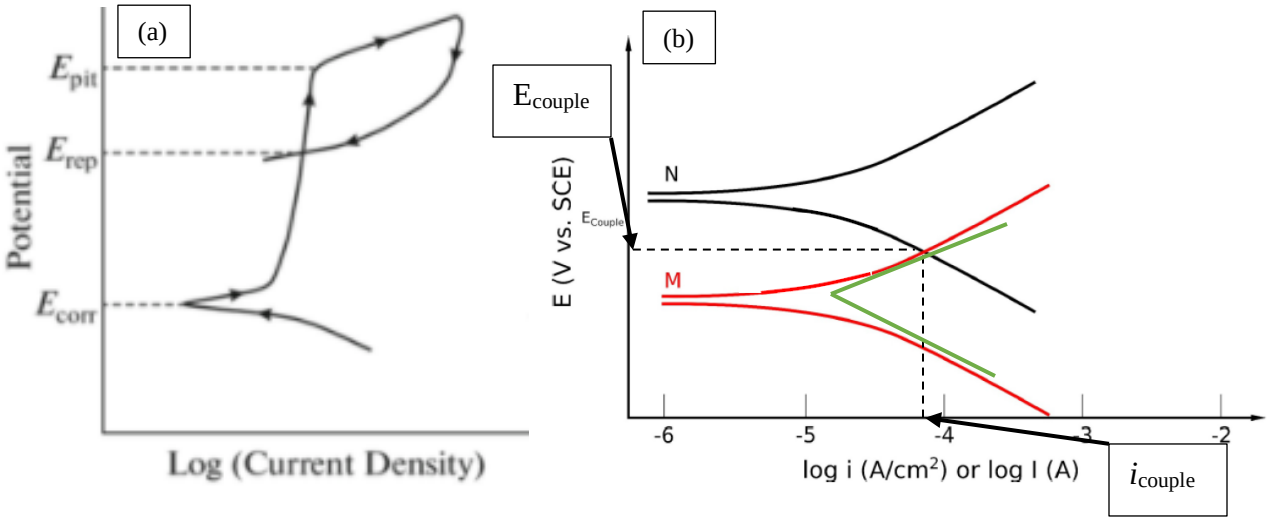

Figure 3. Typical cyclic polarization curve (a) demonstrating pitting potential E_{pit}, corrosion potential E_{corr}, and repassivation potential E_{rep} and (b) of effects of galvanic coupling of metals N and M [2] [7].

At potentials more negative than the open circuit potential, or corrosion potential (E_{corr}), the material will behave as the cathode in the electrochemical cell. In **Figure 3(a)** the portion of the plot below the E_{corr} is where the investigated materials behaved as the cathode. At potentials more positive than the open circuit potential the material will behave as the anode in the electrochemical cell. This can be seen in **Figure 3(a)** as the portion of the plot above the E_{corr}. Some materials may develop a passive film if certain conditions are met. In **Figure 3(a)** on the anodic branch, the potential increases with a constant current density (i). This is indicative of a protective passive film that will inhibit increasing corrosion rates. However, a passivity breakdown may be observed above a certain potential that will lead to pitting corrosion, as seen in **Figure 3(a)** at the E_{pit} portion of the anodic branch. Tangential lines can be drawn along both the anodic and cathodic branches of the curve to calculate the corrosion current density(i_{corr}) and, E_{corr}. The slopes of the tangential lines on the anodic and cathodic branches are called

the Tafel slopes, where β_a is the anodic Tafel slope and β_c is the cathodic Tafel slope. In **Figure 3(b)**, the Tafel slopes are shown in the dark green lines for the metal M. The corrosion rate can be calculated using the following equation:

$$CR\ (mpy) = \frac{0.129 \times i_{corr} \times EW}{\rho} \quad (1)$$

where CR (mpy) is the corrosion rate in mils per year, i_{corr} is the corrosion current density ($\mu A/cm^2$), EW is the equivalent weight of the material (g/equiv), and ρ is the density of the material (g/cm^3).

Figure 3(b) demonstrates the effect of galvanic coupling on the corrosion current density and corrosion potential of the electrochemical cell. This can be observed by the galvanic coupling of materials N and M. The black colored CPP scan demonstrates the uncoupled N material while the red colored CPP scan demonstrates the uncoupled M material. The intersection of the anodic branch of material M and cathodic branch of material N indicate that when galvanically coupled, M will behave as the anode and N will behave as the cathode. This intersection also provides the theoretical corrosion current density of the couple with the coupled corrosion potential, should the areas of both materials be equal.

According to ASTM G71, the coupled galvanic current of the two materials can be measured using a zero-resistance ammeter (ZRA) test. This test involves submerging the two investigated materials of equal dimensions into an aqueous solution connected to the ZRA apparatus. This apparatus will measure the current between the two materials while there is no resistance between them. This allows for a direct measurement of the galvanic coupled current of the two materials without an IR drop across the ammeter. **Figure 4** demonstrates the electrochemical cell setup for a typical ZRA experiment. [2] [8] [9]

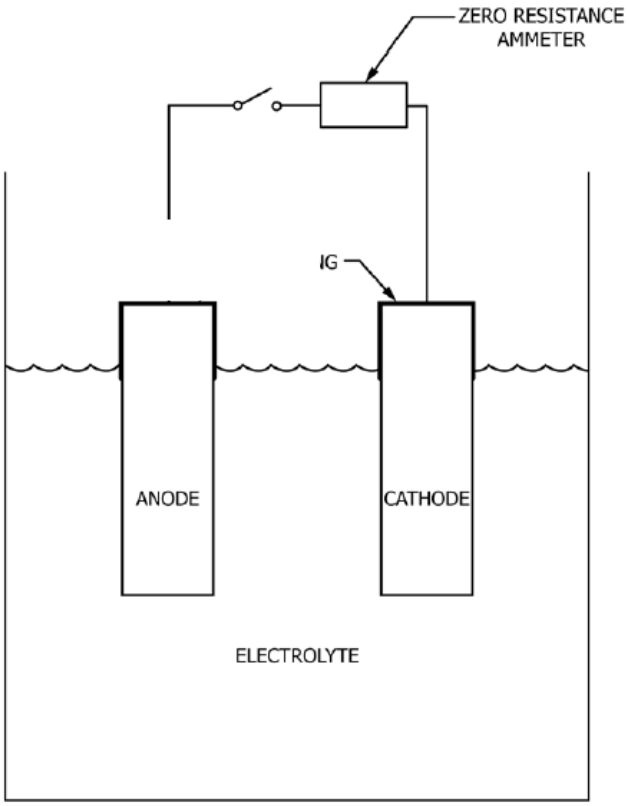

Figure 4. ZRA rest electrochemical cell setup [9].

Electrochemical Impedance Spectroscopy (EIS) is a non-destructive technique that measures polarization resistance by using a small magnitude AC sinusoidal voltage waveform over a range of frequencies. EIS is a very useful method of testing as it can be used to gain a better understanding of the investigated materials corrosion mechanism.

The current that results from the applied sinusoidal potential will in response be sinusoidal in nature, however it will shift in its phase. The sinusoidal current and potential can be expressed using the following equations:

$$I_t = I_0 \times \sin(\omega t + \theta) \quad (2)$$

$$E_t = E_0 \times \sin(\omega t) \quad (3)$$

where ω is the radial frequency, θ is the shift in phase of the current, I_o is the current amplitude, I_t is the current at time t, E_o is the potential amplitude, and E_t is the potential at time t. From these relationships' impedance, Z, can be calculated through the following equation:

$$Z = \frac{E_t}{I_t} = \frac{E_o \times \sin(\omega t)}{I_t \times \sin(\omega t + \theta)} = Z_o \frac{\sin(\omega t)}{\sin(\omega t + \theta)} \quad (4)$$

Using Equation (4) and Euler's relationship, the following expression can be used to describe impedance as a complex number:

$$Z(\omega) = \frac{E}{I} = Z_o[\cos(\theta) + j\sin(\theta)] \quad (5)$$

As a result, the impedance can be expressed in terms of real and imaginary components:

$$Z(\omega) = Z'(\omega) + Z''(\omega) \quad (6)$$

With *Z'(ω)* corresponding to the real component, and *Z''(ω)* corresponding to the imaginary component. These expressions plotted on a Nyquist plot or Bode Plot, see **Figure 5**.

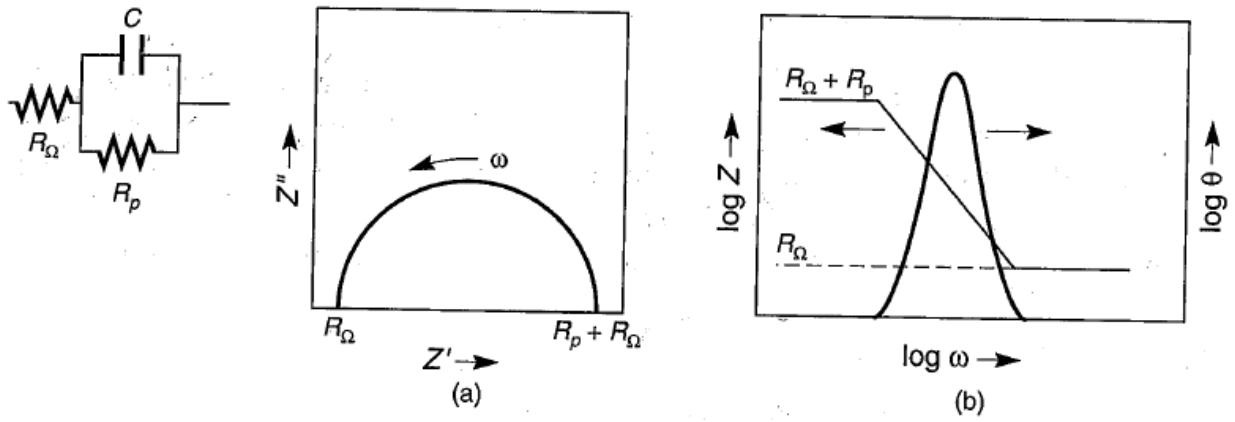

Figure 5. Example Nyquist plot and Bode plot. [2]

These plots can be used to propose an equivalent electrical circuit (EEC) that is closely approximate to the capacitive or resistive components occurring on the materials surface. The solution resistance can also be

approximated from the plots. In uncoated specimens, a Randles' circuit (see **Figure 6(a)** or **Figure 5**) is typically used to model the equivalent circuit due to its simplicity and investigation of solely polarization resistance and double layer capacitance. In **Figure 6** example equivalent electrical circuit examples can be seen. [2] [5] [10−13]

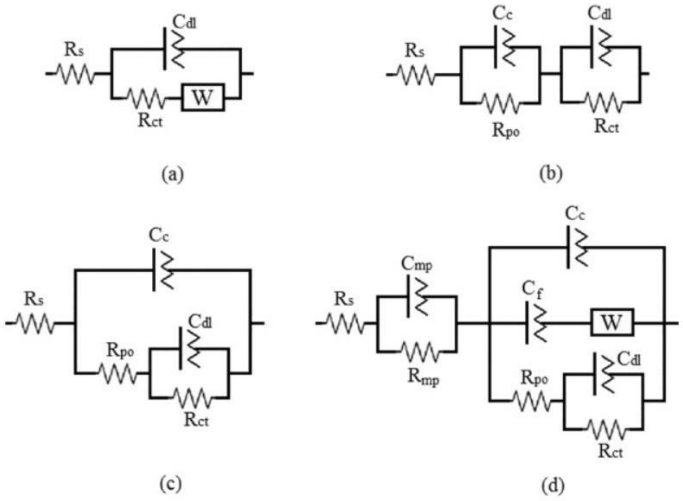

Figure 6. Example equivalent electrical circuits.

Rotating disk electrode (RDE) tests affect the thickness of the diffusion double layer by affecting the flow regime at the interface of the material and solution. These tests are effective at investigating how mass transport is affected at different flow velocities. For this purpose, higher solution flow speeds may simulate the effect of atmospheric corrosion by reducing the diffusional layer at the material interface to the desired thickness.

The kinetics of the corrosion current density under this controlled diffusion layer can best be described using the Levich equation. This equation describes the limiting current density as a function of the bulk concentration, diffusivity, kinematic viscosity, and angular velocity.

$$i_L = 0.620 \times n \times F \times D_Z^{\frac{2}{3}} \times \omega^{\frac{1}{2}} \times v^{-\frac{1}{6}} \times C_B \qquad (7)$$

where n is the amount of moles of electrons transferred, F is the Faraday constant, D_z is the diffusivity of the reacting species, ω is the angular velocity (rads/time), v is the kinematic viscosity, and C_B is the bulk solution concentration of the reacting species. [2] [5] [14]

Scanning Kelvin probes (SKP) are a test method that involves a Kelvin probe measuring the surface electrical potential of the investigated specimen. The surface potential of the specimens is measured by first placing the probe tip close to the specimen, however not in contact. This will in effect act as a capacitor between the probe tip and sample. As the potential difference between the probe and sample generates a buildup of charge on the probe tip, the probe tip will oscillate to vary the distance between the two. This oscillation will adjust the capacitance and in turn the current on the probe tip that can be measured. This can best be described through the following relationship and **Figure 7**:

$$C_k(t) = \frac{\varepsilon_0 A}{d(t)}\ ,\ d(t) = d_0 + d_1 \cos(\omega t) \qquad (8)$$

Where d_0 is the distance between the sample to the probe tip, and d_1 is half the probe oscillation amplitude.

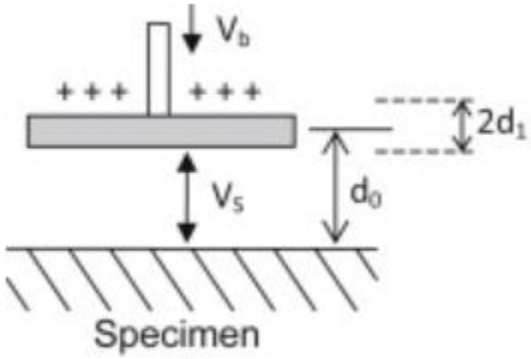

Figure 8. Schematic of Kelvin probe tip in relation to specimen [15-18]

For this project zero-resistance ammeter tests on carbon steel 1018 with AA6022 and AA6111 were performed in addition to the materials uncoupled in both 0.6M NaCl and 0.06M NaCl solution. CPP and EIS tests were performed during RDE experiments in both 0.6M NaCl and 0.06M NaCl solutions. Rotating disk electrode were utilized to simulate the effects of atmospheric conditions when performing the CPP and EIS experiments. The RDE tests will be performed at 0, 100, 500, 1000, and 2000 rotations per minute (rpm). A Scanning Kelvin Probe (SKP) will be used to characterize the coupled materials potential gradient. The resulting data will be used to generate a clear understanding on the corrosion mechanism and kinetics of the galvanic coupling of the materials involved in simulated atmosphere environments.

Experimental Methods

Sample Preparation

The carbon steel 1018, AA6022, and AA6111 samples were prepared by cutting 1 x 1 cm squares from the respective materials sheets. The area of the samples was 1 cm^2. Solutions of 0.06M and 0.6M NaCl were prepared prior to testing in 2L volumetric flasks. For testing purposes, excluding RDE experiments, the test specimens were mounted in epoxy resin prior to electrochemical testing. For RDE experiments, the individual test specimens were mounted on a 3D printed in-house apparatus due to insufficient equipment and sample preparation issues. Upon completion of mounting, the samples were polished step wise starting from 180, 360, 600, and 1200 SiC grinding paper. Upon completion of the 1200 SiC polish the samples were rinsed with deionized water, then ethanol to air dry.

Sample Exposure and Testing

ZRA tests were performed in a three-electrode electrochemical cell, with one metal acting as a working electrode (WE), another galvanically coupled metal as the counter electrode (CE) and saturate calomel electrode (SCE) as the reference electrode (RE). This test was performed in both 0.6M NaCl and 0.06M NaCl solutions without the simulation of atmospheric conditions. The tests were performed with a duration of 10,800 seconds and a sample period of 1 second in accordance with ASTM G71. Each test was repeated twice to verify results and reproducibility. The test matrix for all ZRA test conditions can be seen in **Table 1**:

Table 1. ZRA Test Matrix.

Test Materials	Solution
AA6111	0.6M NaCl, 0.06M NaCl
AA6111 Coupled with CS	0.6M NaCl, 0.06M NaCl
AA6022	0.6M NaCl, 0.06M NaCl
AA6022 Coupled with CS	0.6M NaCl, 0.06M NaCl
CS	0.6M NaCl, 0.06M NaCl

During the RDE experiments a typical three-electrode setup was used to perform the experimentation, using the studied alloy as the WE, graphite as the CE, and SCE as the RE. During the RDE experiments, the material was stabilized to OCP upon 1 hour, with EIS and CPP tests performed sequentially upon completion of

OCP. The tests were performed in 0.6M NaCl and 0.06M NaCl solutions. The rotational speed was varied to determine the effect of the flow regime on the double layer capacitance of the galvanically coupled materials and simulate various atmospheric environments. The rotational speeds investigated were 0, 100, 500, 1000, and 2000 rpm. Each test was repeated twice to verify results and reproducibility. **Table 2** provides the test sequence and parameters for the RDE experiments.

Table 2. RDE Test Sequence and Parameters.

OCP	EIS	CPP
Duration: **3,600 s**	Frequency: **1 – 10 MHz**	Scan Range: **±800 mV**
Sample Period: **1 s**	Steps/Decade: **10**	Scan Rate: **2 mV/s**
Sample Area: **0.1963 cm^2**	Potential: **10 mV (rms)**	Sample Period: **1 s**
	Sample Area: **0.1963 cm^2**	Sample Area: **0.1963 cm^2**

The test matrix for all RDE test conditions can be seen in **Table 3**:

Table 3. RDE Testing Matrix.

Test Materials	Solution	Rotational Speed (RPM)
AA6111	0.6M NaCl	0, 100, 500, 1000, 2000
AA6111	0.06M NaCl	0, 100, 500, 1000, 2000
AA6022	0.6M NaCl	0, 100, 500, 1000, 2000
AA6022	0.06M NaCl	0, 100, 500, 1000, 2000
CS	0.6M NaCl	0, 100, 500, 1000, 2000
CS	0.06M NaCl	0, 100, 500, 1000, 2000

Scanning Kelvin Probe (SKP) tests were performed on galvanically coupled materials to map the surface potential gradient on galvanically coupled materials. The investigated materials were polished to 1200 grit finish galvanic coupled CS1018 with AA6111 and CS1018 with AA6022. In addition to these specimens, oxidized samples of the two coupled specimens were prepared by immersion testing for 5 hours in accordance with ASTM G31 [19].

The SKP scan was performed in an enclosed chamber with a relative humidity that ranged between 85%-90%. The SKP tests were performed upon initial placement in the chamber and repeated upon 50 minutes exposure in the chamber.

Upon completion of tests, an optical microscope was used to perform an analysis on the corrosion products of the exposed specimens. Further investigation of specimens was performed utilizing scanning electron microscopy (SEM). Energy dispersive x-ray (EDX) analysis was used to study the elemental composition of the formed corrosion products and its distribution among the galvanic coupled area.

Data and Results

ZRA tests were performed on the coupled materials in 0.6M NaCl and 0.06M NaCl solutions in order to measure and compare the galvanic coupled current.

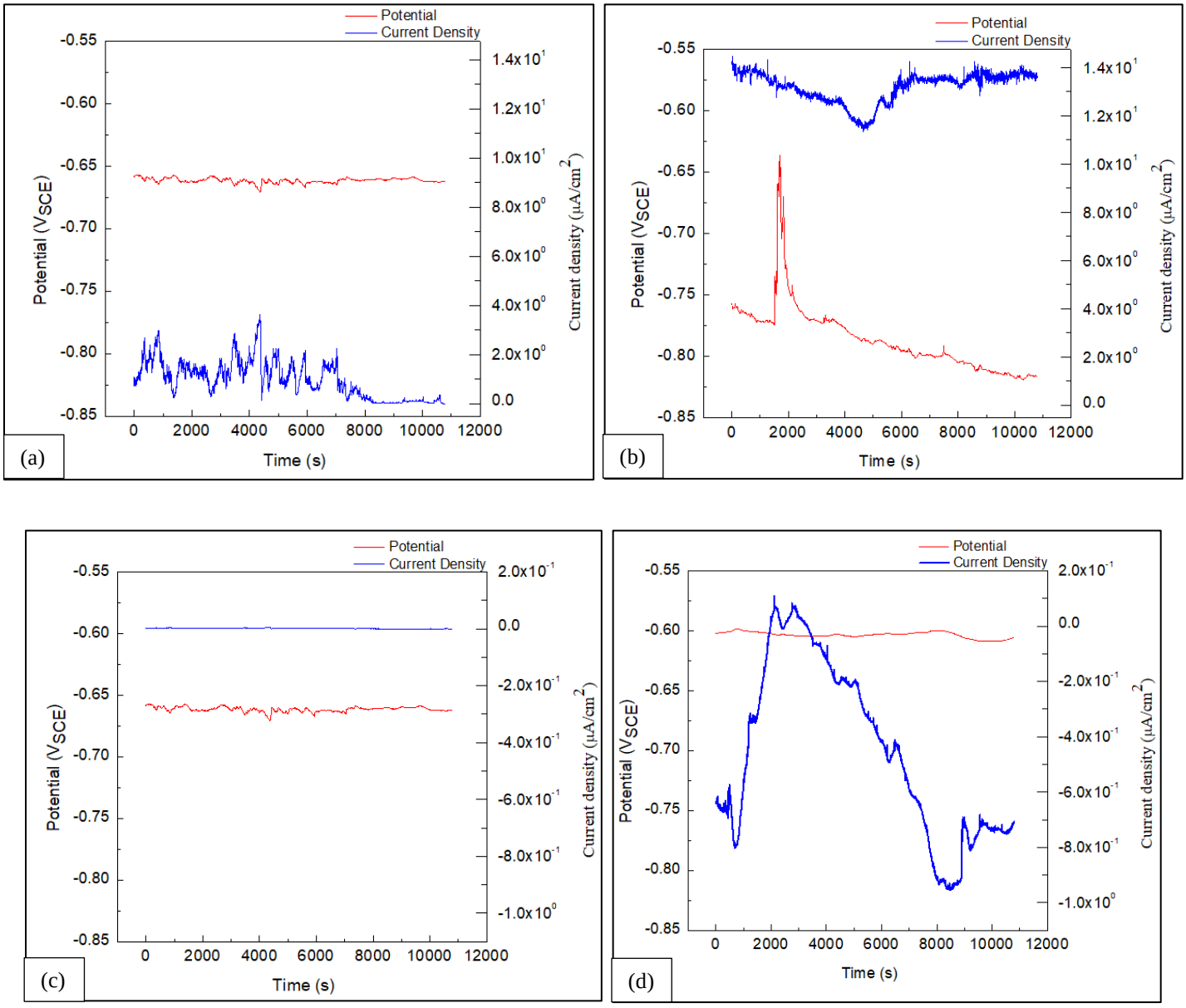

Figure 9. ZRA plot of CS1018 and AA6111 in (a) (b) 0.6M NaCl and (c) (d) 0.06M NaCl

From **Figure 9**, the stabilization of current density and potential between the CS1018 and AA6111 is shown with respect to time. The first set of tests shown in **Figures 9(a)** and **9(c)** demonstrate that in 0.6M NaCl and 0.06M NaCl the galvanic coupled current density is 8.707×10^{-3} μA/cm^2 and 8.707×10^{-6} μA/cm^2 respectively.

These values are indicative of minor galvanic coupling effect between the two materials. This conflicts with previous literature and theorizations. The second set of tests shown in **Figures 9(b)** and **9(d)** demonstrate the galvanic coupled current density is 1.358 x 10^{1} μA/cm^2 and -7.080 x 10^{-1} μA/cm^2 in 0.6M NaCl and 0.06M NaCl respectively. These values reinforce that there was minor galvanic coupling between CS1018 and AA6111 in both solutions. See **Table 4** for all quantitative values.

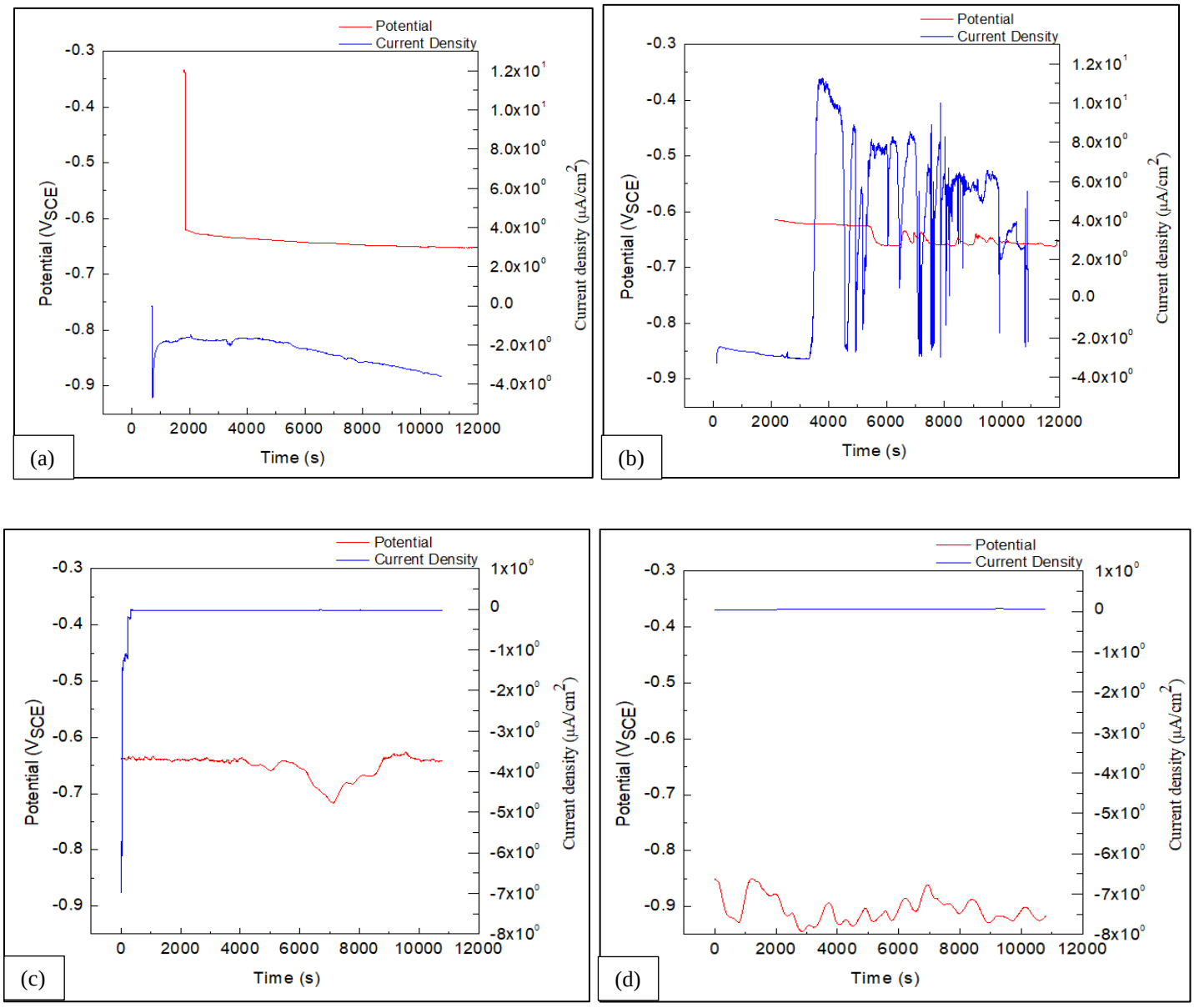

Figure 10. ZRA plot of CS1018 and AA6022 in (a) (b) 0.6M NaCl and (c) (d) 0.06M NaCl

From **Figure 10**, the stabilization of current density and potential between the CS1018 and AA6022 is demonstrated with respect to time. The first set of tests shown in **Figures 10(a)** and **10(c)** demonstrate that in 0.6M NaCl and 0.06M NaCl the galvanic coupled current density is -3.59 $\mu A/cm^2$ and -2.819 x 10^{-2} $\mu A/cm^2$ respectively. These values are indicative of minor galvanic coupling effect between the two materials. The second set of tests shown in **Figures 10(b)** and **10(d)** demonstrate the galvanic coupled current density is -2.040 $\mu A/cm^2$ and 6.359 x 10^{-2} $\mu A/cm^2$ in 0.6M NaCl and 0.06M NaCl respectively. Such values are, again, inconclusive in addition to the first set of tests in concluding that a galvanic couple is present. More testing should be performed on both sets of coupled materials to provide more conclusive results. See **Table 4** for all quantitative values.

Table 4. Quantitative final values of coupled CS1018 with AA6111 and CS1018 with AA6022

Solution	**Parameter**	**CS1018 and AA6111**				**CS1018 and AA6022**			
		Test 1	Test 2	**Average**	**St. Dev.**	Test 1	Test 2	**Average**	**St. Dev.**
0.6M NaCl	*i* ($\mu A/cm^2$)	8.707 x 10^{-3}	1.358 x 10^{1}	**6.794**	**0.0096**	-3.590	-2.040	**-2.815**	**0.0011**
	E (V_{SCE})	-0.662	-0.817	**-0.740**	**0.1096**	-0.653	-0.650	**-0.652**	**0.0021**
0.06M NaCl	*i* ($\mu A/cm^2$)	8.707 x 10^{-6}	-7.080 x 10^{-1}	**-3.540 x 10^{-1}**	**0.0005**	-2.819 x 10^{-2}	6.359 x 10^{-2}	**1.770 x 10^{-2}**	**0.0001**
	E (V_{SCE})	-0.662	-0.606	**-0.634**	**0.0396**	-0.643	-0.917	**-0.780**	**0.1937**

Upon completion of the 10800 seconds (3 hours) exposure to both 0.6M NaCl and 0.06M NaCl solutions from the ZRA experiments, all specimens were characterized under an optical microscope.

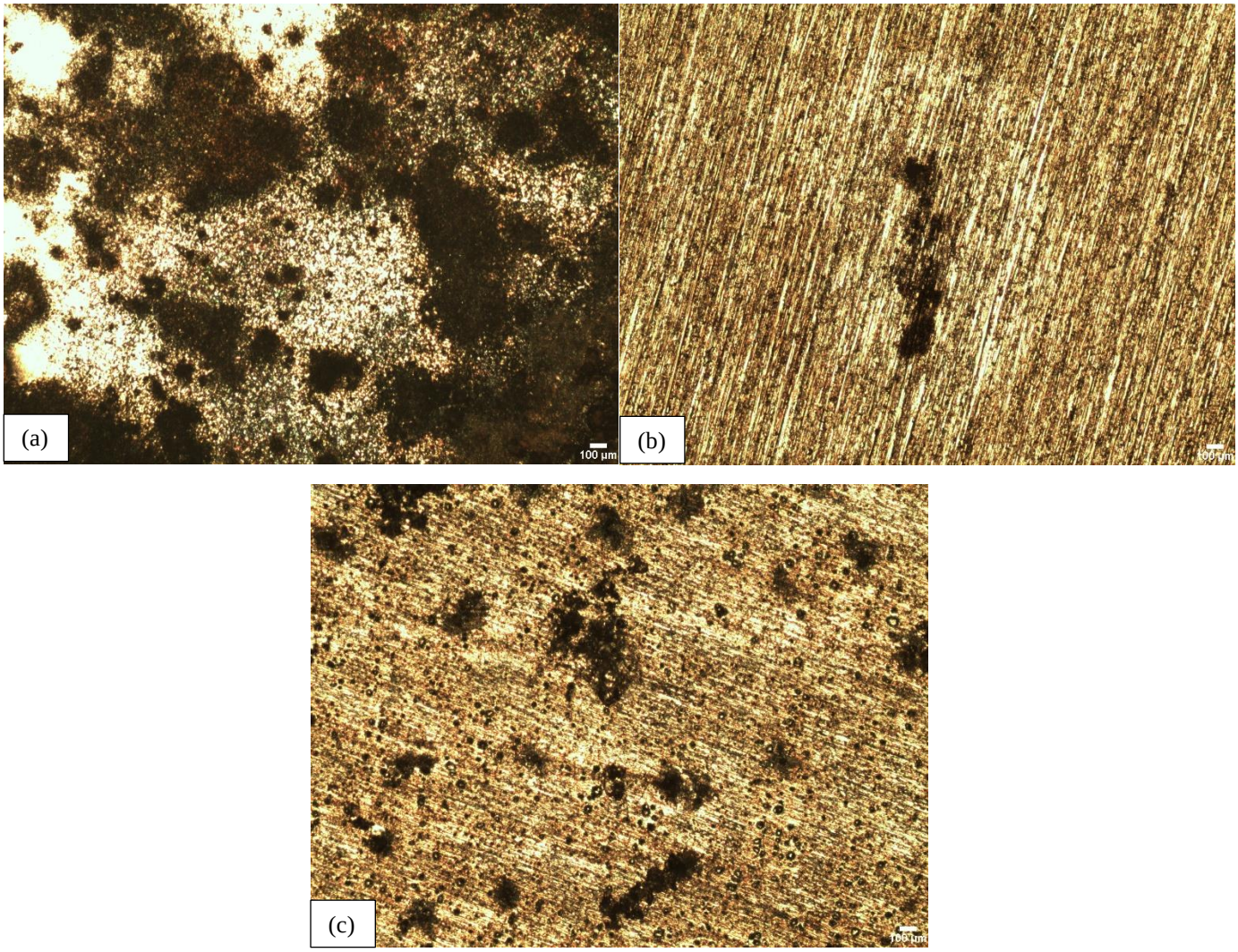

Figure 11. Optical Microscope images of individual (a) CS1018, (b) AA6111, and (c) AA6022 upon completion of 24-hour immersion in 0.6M NaCl at 5x Magnification.

Individual specimens of CS1018, AA6111, and AA6022 we immersed in 0.6M NaCl in accordance with the procedure for the ZRA test. In **Figure 11(a)** large-scale pitting can be observed in the CS1018 sample. In **Figure 11(b)** and **Figure 11(c)** pitting did occur on AA6111 and AA6022 upon completion of testing.

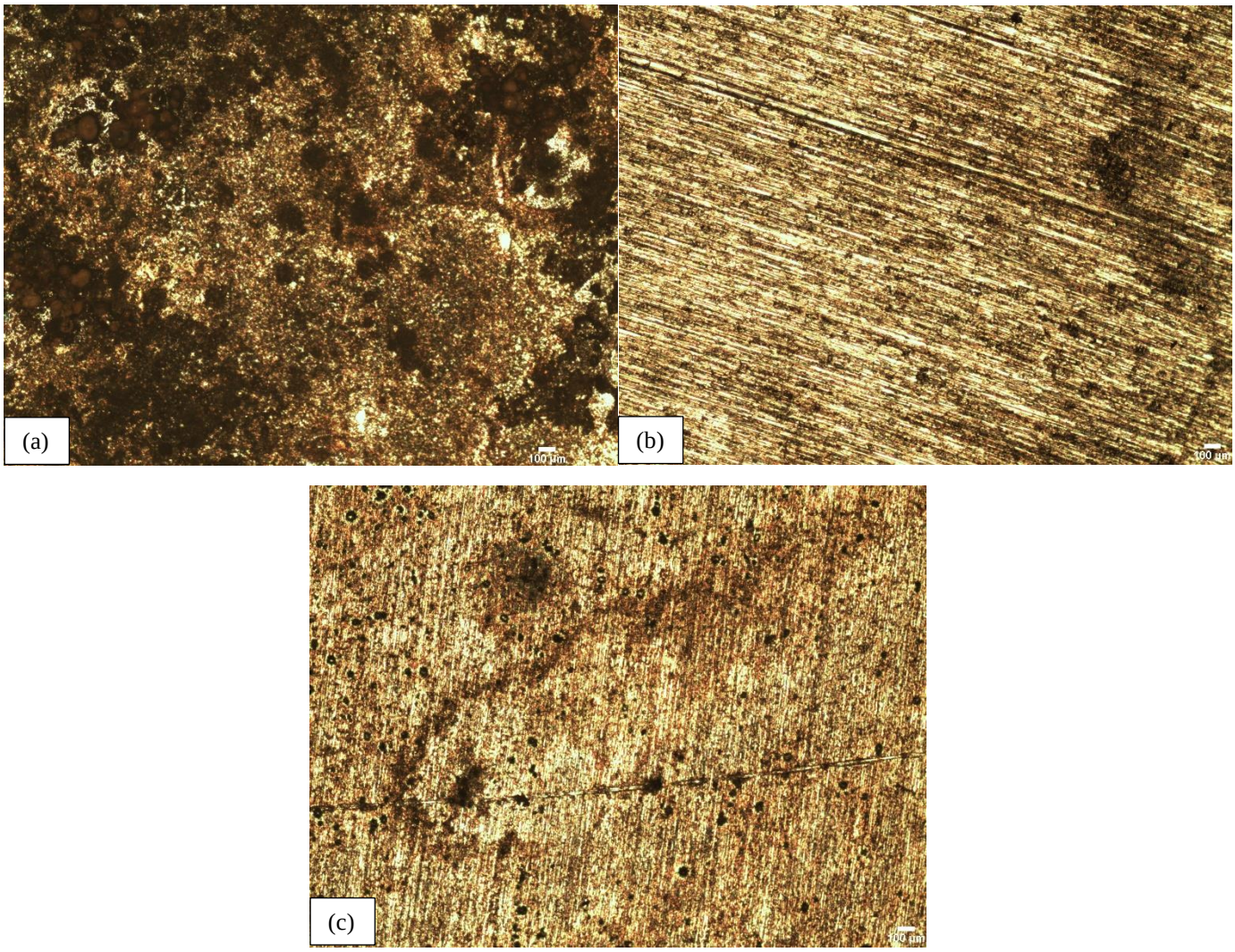

Figure 12. Optical Microscope images of (a) CS1018, (b) AA6111, and (c) AA6022 upon completion of 24-hour immersion in 0.06M NaCl at 5x Magnification.

Individual specimens of CS1018, AA6111, and AA6022 we immersed in 0.06M NaCl in accordance with the procedure for the ZRA test. In **Figure 12(a)** large-scale pitting can be observed in the CS1018 sample. In **Figure 12(b)** and **Figure 12(c)** minor pitting did occur on AA6111 and AA6022 upon completion of testing.

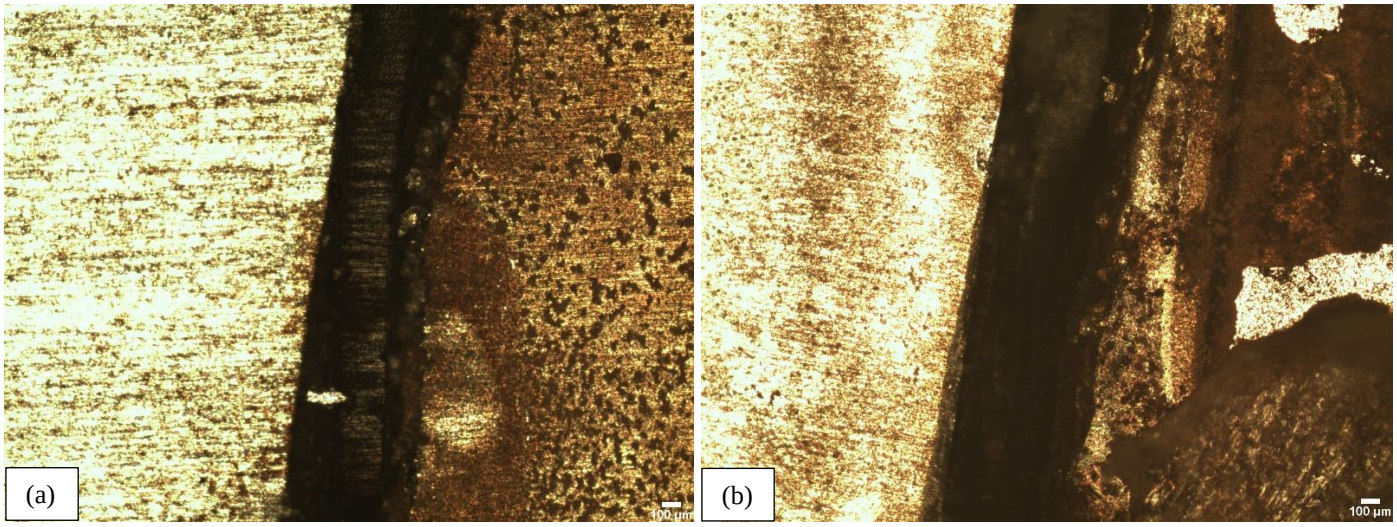

Figure 13. Optical Microscope images of (a) AA6111 (Left) and CS1018 (Right) after 0.6M NaCl ZRA test, and (b) AA6111 (Left) and CS1018 (Right) after 0.06M NaCl 24-hour immersion at 5x Magnification.

Galvanic coupled CS1018 and AA6111 demonstrated enhanced corrosion product formation along the interface between the two materials upon completion of ZRA testing. In 0.6M NaCl, see **Figure 13(a)**, CS1018 developed more uniform pitting along the interface while AA6111 failed to demonstrate any indication of corrosion occurring at the interface in 0.6M NaCl. In 0.06M NaCl, see **Figure 13(b)**, CS1018 provided an enhanced corrosion product formation at the interface, in comparison with the uncoupled image of CS1018 in **Figure 12(a)**, while AA6111 remained intact.

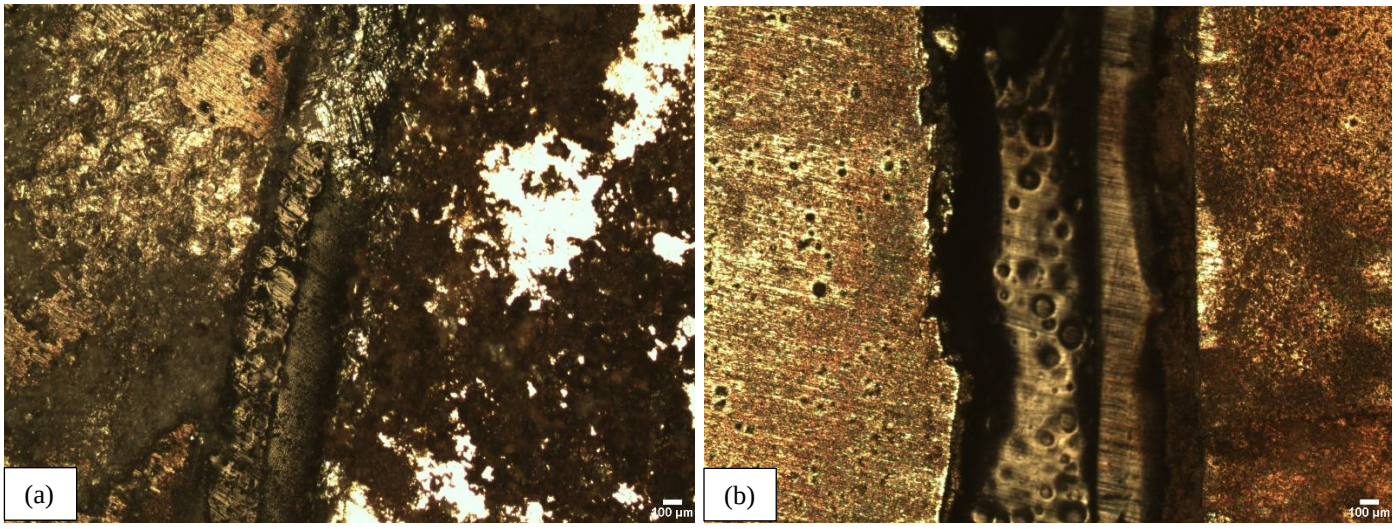

Figure 14. Optical Microscope images of (a) AA6022 (Left) and CS1018 (Right) after 0.6M NaCl ZRA test, and (b) AA6022 (Left) and CS1018 (Right) after 0.06M NaCl 24-hour immersion at 5x Magnification.

Galvanic coupled CS1018 and AA6022 proved more difficult to characterize. In 0.6M NaCl, see **Figure 14(a)**, the CS1018 did demonstrate enhanced corrosion product formation along the interface. However, AA6022 also provided an enhanced corrosion product formation along the interface. Both materials show an increased severity of corrosion in comparison with the uncoupled images from **Figure 12**. In 0.06M NaCl, see **Figure 14(b)**, CS1018 demonstrated enhanced corrosion product formation along the interface while the AA6022 displayed limited pitting.

To better understand the kinetics of each individual material in the atmospheric environment, CPP and EIS experiments were performed at 0, 100, 500, 1000, and 2000 rpm in both 0.6M NaCl and 0.06M NaCl.

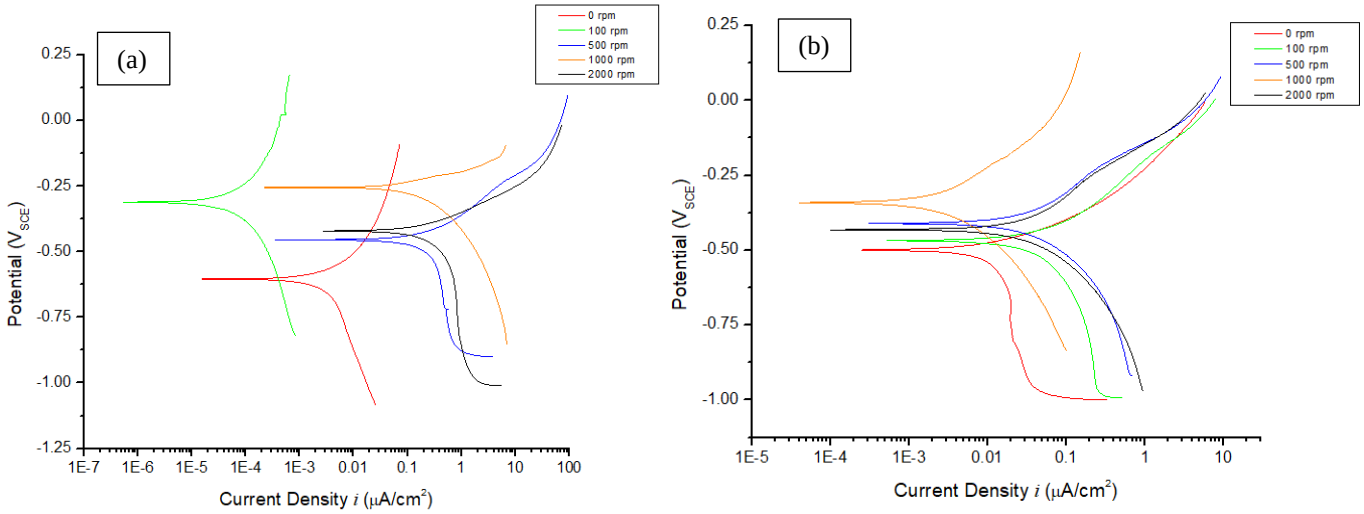

Figure 15. CPP curve of CS1018 in (a) 0.6M NaCl and (b) 0.06M NaCl at 0, 100, 500, 1000 and 2000 rpm.

In **Figure 15** the effect of the resultant diffusion layer from the rotational speed on the corrosion current density in CS1018 can be observed. At higher rotational speeds, the corrosion current density increased, in comparison with lower rotational speeds and the stagnant experiment. The corrosion potential for the CS1018 was more electropositive than the coupled corrosion potential from the previous ZRA experiments. This is indicative of the carbon steel behaving as the cathode in the galvanic couple (see **Table 4**). Inconsistencies with the rotational speed, in terms of trend, may be due to poor surface finish of the sample or issues with connection of the Gamry potentiostat.

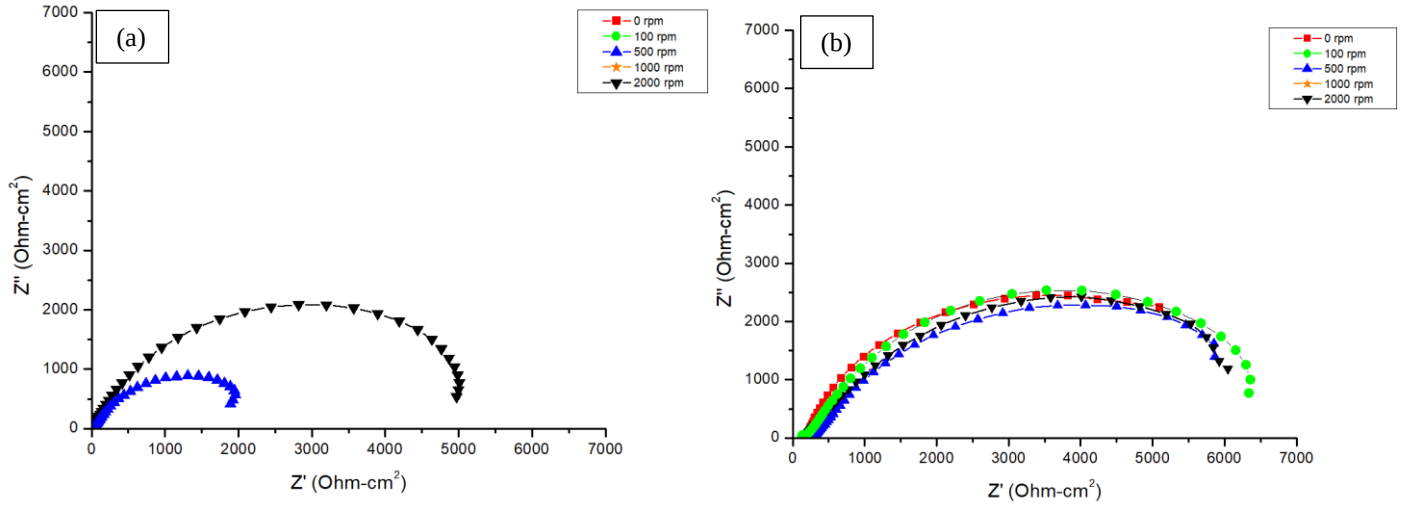

Figure 16. Nyquist plot of CS1018 in (a) 0.6M NaCl and (b) 0.06M NaCl at 0, 100, 500, 1000 and 2000 rpm.

The equivalent circuit used to model the EIS data was determined to be a Randles' circuit. The generated EIS plots demonstrated a single time constant. This model provided an adequate fitting of the data. In **Figure 16(a)** there was an observable difference between rotational speed and polarization resistance in 0.6M NaCl. In **Figure 16(b)** no such difference in polarization resistance with increasing rotational speed was observed in 0.06M NaCl. Due to experimental error from poor sample surface finish or issues with connection to the Gamry potentiostat, not all rotational speeds are included in the plot. Reproduction of such experiments were limited due to time constraints.

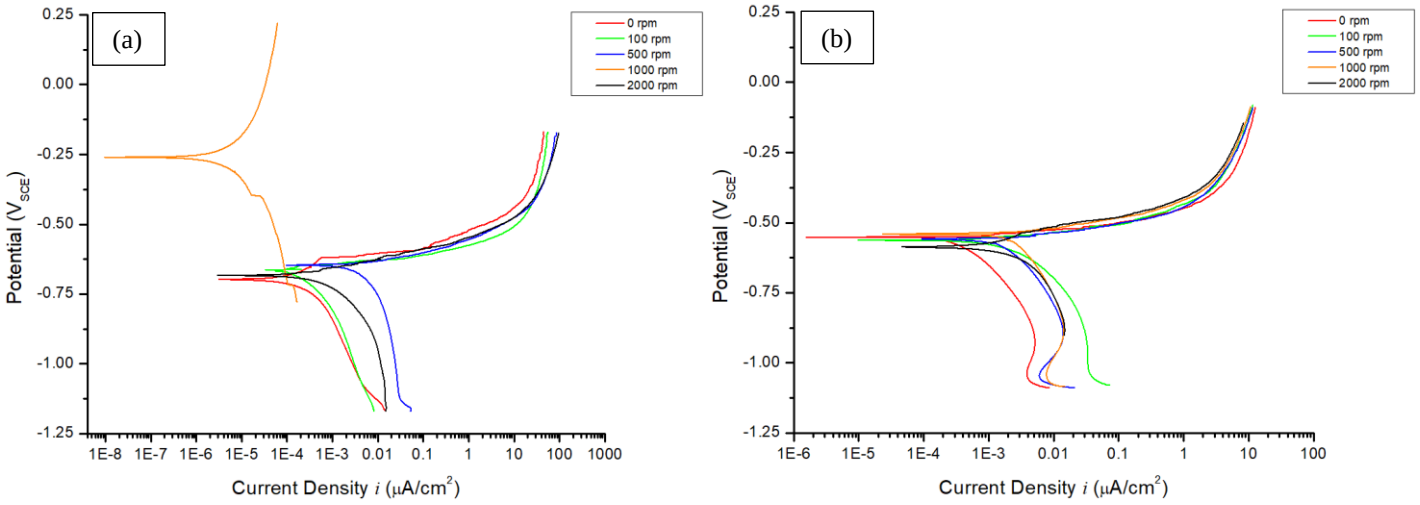

Figure 17. CPP curve of AA6111 in (a) 0.6M NaCl and (b) 0.06M NaCl at 0, 100, 500, 1000 and 2000 rpm.

In **Figure 17** the effect of the resultant diffusion layer from the rotational speed on the corrosion current density in AA6111 can be observed. With the exception of 500 rpm in 0.6M NaCl, at higher rotational speeds the corrosion current density increased, in comparison with lower rotational speeds and the stagnant experiment. The corrosion potential for the AA6111 was approximately equal to the coupled corrosion potential from the previous ZRA experiments. This is indicative of the aluminum alloy behaving as the anode in the galvanic couple (see **Table 4**). In **Figure 17(a)**, the 1000 rpm experiment in 0.6M NaCl is not consistent with the trend due to poor surface finish or connection issues with the Gamry potentiostat.

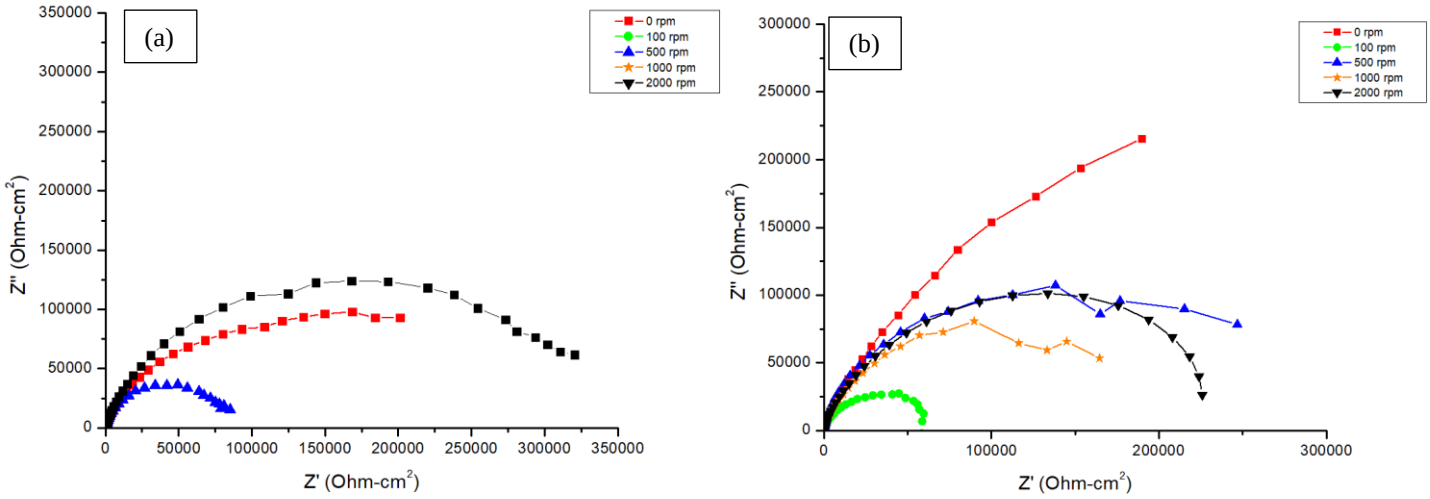

Figure 18. Nyquist plot of AA6111 in (a) 0.6M NaCl and (b) 0.06M NaCl at 0, 100, 500, 1000 and 2000 rpm.

In **Figure 18(a)** and **Figure 18(b)** there was an observable difference between rotational speed and polarization resistance in 0.6M NaCl and 0.06M NaCl. No identifiable trend was found that correlated polarization resistance to rotational speed. Due to experimental error from poor sample surface finish or issues with connection to the Gamry potentiostat, not all rotational speeds are included in the plot. Reproduction of such experiments were limited due to time constraints.

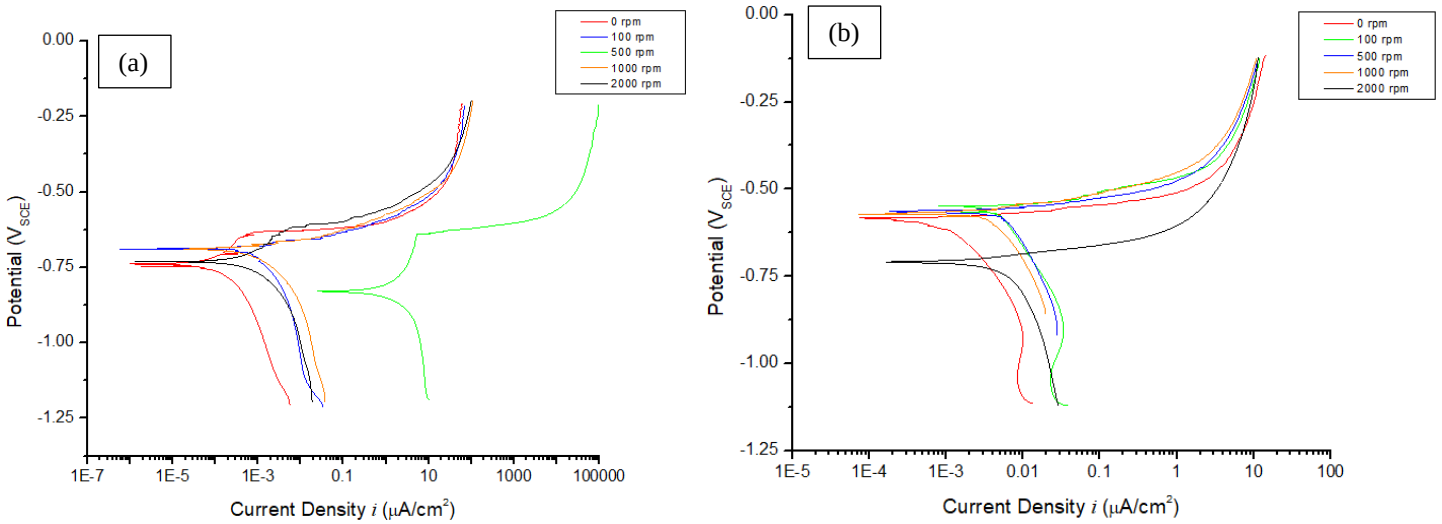

Figure 19. CPP curve of AA6022 in (a) 0.6M NaCl and (b) 0.06M NaCl at 0, 100, 500, 1000 and 2000 rpm.

In **Figure 19** the effect of the resultant diffusion layer from the rotational speed on the corrosion current density in AA6022 can be observed. At higher rotational speeds, the corrosion current density increased, in comparison with lower rotational speeds and the stagnant experiment. The corrosion potential for the AA6022 was approximately equal to the coupled corrosion potential from the previous ZRA experiments. This is indicative of the aluminum alloy behaving as the anode in the galvanic couple (see **Table 4**).

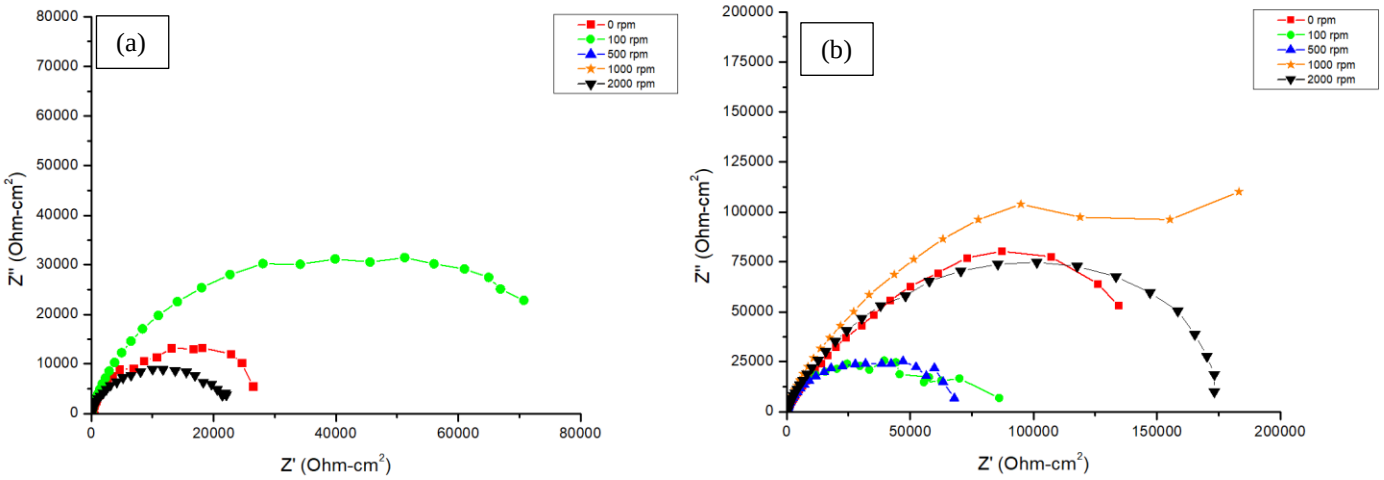

Figure 20. Nyquist plot of AA6022 in (a) 0.6M NaCl and (b) 0.06M NaCl at 0, 100, 500, 1000 and 2000 rpm.

In **Figure 20(a)** and **Figure 20(b)** there was an observable difference between rotational speed and polarization resistance in 0.6M NaCl and 0.06M NaCl. No identifiable trend was found that correlated polarization resistance to rotational speed. Due to experimental error from poor sample surface finish or issues with connection

to the Gamry potentiostat, not all rotational speeds are included in the plot. Reproduction of such experiments were limited due to time constraints.

The corrosion behavior of AA6022 was the best performing alloy in 0.6M NaCl over AA6111 and CS1018. It demonstrated nearly a 3x magnitude lower i_{corr} when compared to CS1018 and AA6111. The E_{corr} of AA6022 in 0.6M NaCl also demonstrated to be the most negative when compared to AA6111 and CS1018.The corrosion behavior of AA6022 and CS1018 demonstrated to better performing in 0.06M NaCl when compared to AA6111. Both CS1018 demonstrated similar i_{corr} and E_{corr} in 0.06M NaCl. AA6111 demonstrated a more electropositive E_{corr} and a magnitude greater i_{corr} compared to AA6022 and CS1018 in 0.06M NaCl.

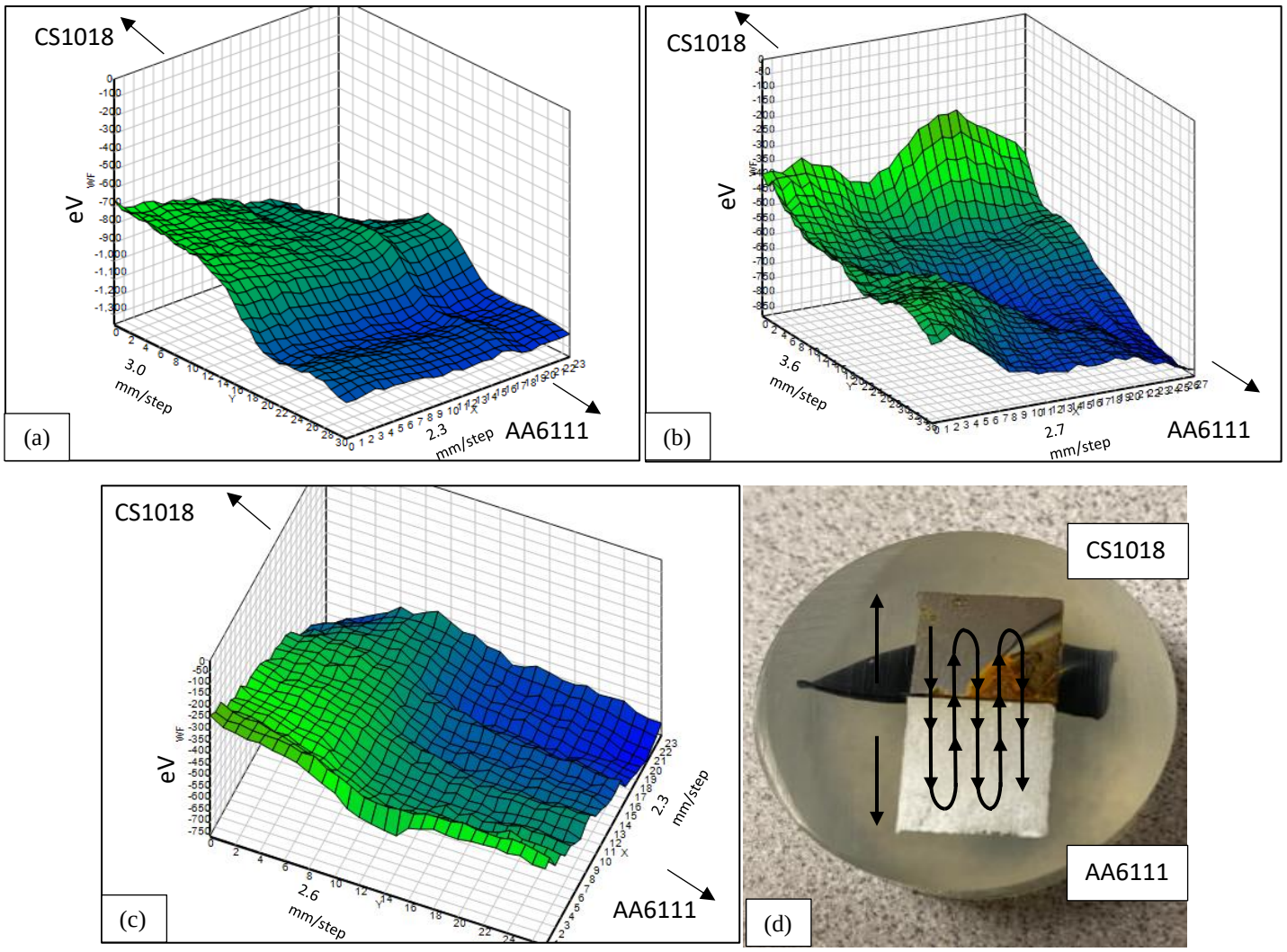

Figure 21. SKP mapping of galvanic coupling potential gradient of CS1018 (Green) and AA6111 (Blue) after (a) No Exposure, (b) 5 Hour Exposure 0.6M NaCl, and (c) 5 Hour Exposure 0.06M NaCl. (d) Example sample layout and scan pathway.

In **Figure 21**, the scan of CS1018 and AA6111 can be observed. The specimens were electrically isolated at the CS1018 and AA6111 interface in order to prevent the formation of a crevice during testing. There is a definite observable change in potentials of the specimens, with AA6111 behaving slightly more negative than CS1018. The significant dip in potential pertains to the electrically isolated interface between the two specimens in the epoxy resin. In **Figure 21(b)** after an exposure of 5 hours in 0.6M NaCl, a positive increase in the potential of the CS018 can be observed in comparison with other scans. This is possibly due to the formation of corrosion products on the surface.

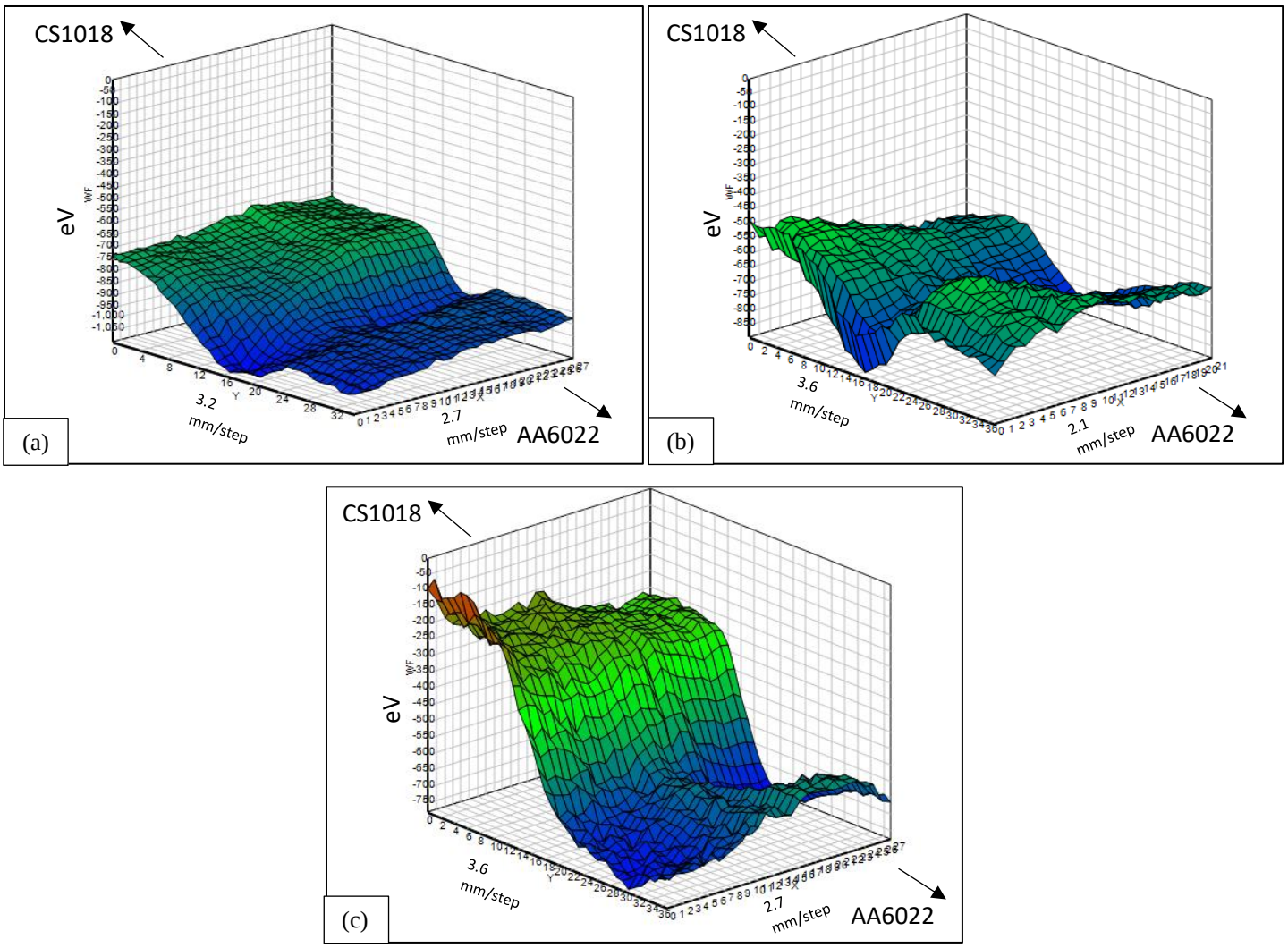

Figure 22. SKP mapping of galvanic coupling potential gradient of CS1018 (Green) and AA6022 (Blue) after (a) No Exposure, (b) 5 Hour Exposure 0.6M NaCl, and (c) 5 Hour Exposure 0.06M NaCl.

In **Figure 22**, the scan of CS1018 and AA6022 can be observed. There is a definite change in potentials of the specimens, with AA6022 behaving slightly more negative than CS1018. The significant dip in potential pertains to the electrically isolated interface between the two specimens in the epoxy resin.

SEM and EDX characterization were performed on the specimens upon completion of ZRA experimentation.

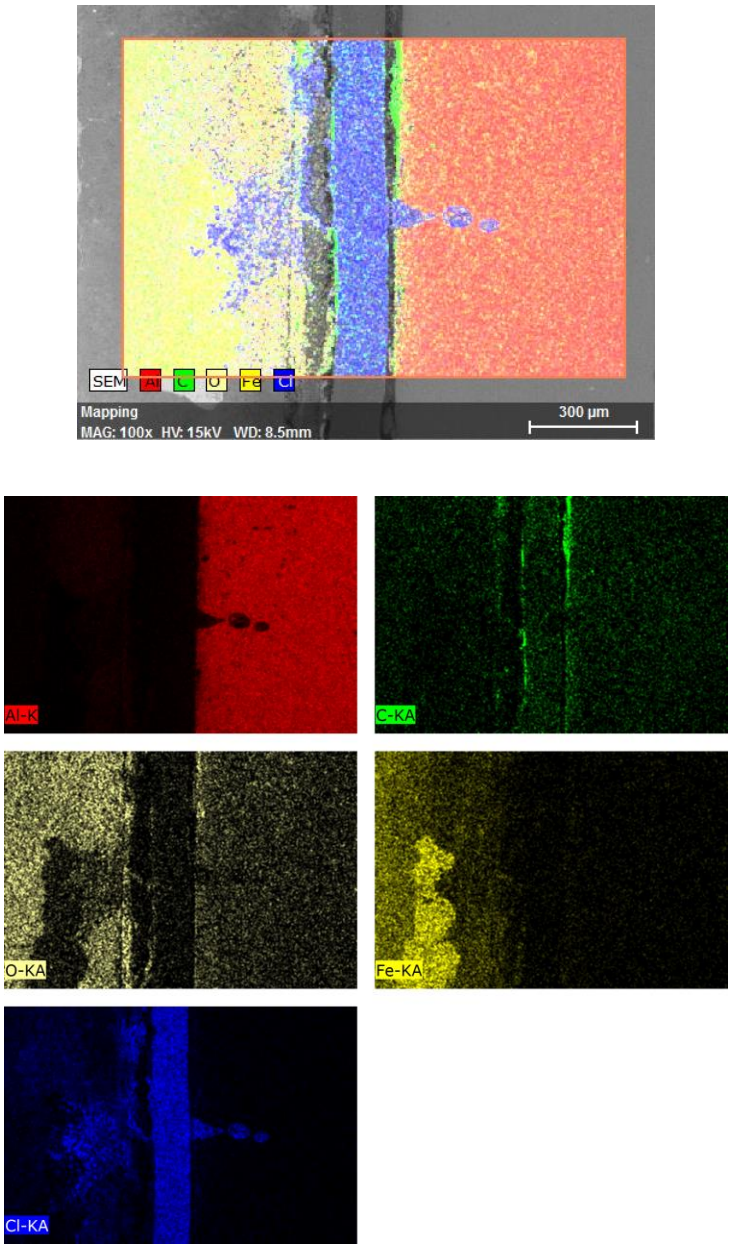

Figure 23. SEM image and EDX mapping of CS1018 (Left) and AA6111 (Right) after 3-hours immersion in 0.6M NaCl from ZRA experimentation.

SEM characterization of CS1018 coupled with AA6111 after a 3 hour exposure in 0.6M NaCl demonstrated that the galvanic couple severely impacts the corrosion rate of the CS1018 when coupled. The aluminum, seen in **Figure 23**, can be observed to demonstrate little to no formation of corrosion products on the surface. However, the oxygen content on the CS1018 sample is much larger than that on the aluminum alloy. The formation of an oxide layer on the CS1018 reinforces that it behaved as the anode in the galvanic couple.

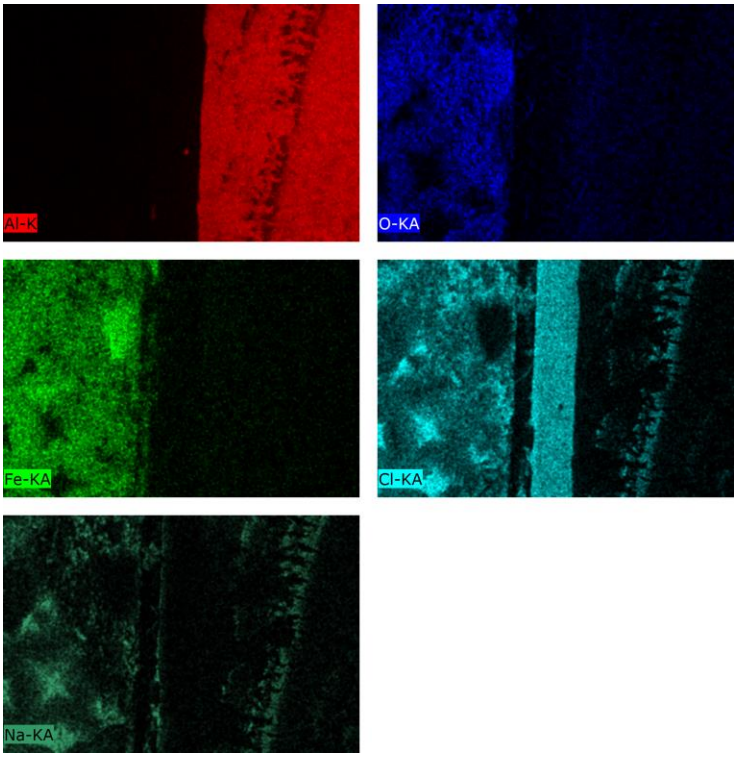

Figure 24. SEM image and EDX mapping of CS1018 (Left) and AA6022 (Right) after 3-hours immersion in 0.6M NaCl from ZRA experimentation.

SEM characterization of CS1018 coupled with AA6022 after a 3 hour exposure in 0.6M NaCl demonstrated that the galvanic coupled severely impacts the corrosion rate of the CS1018 when coupled. The aluminum, seen in **Figure 24**, can be observed to demonstrate little to no formation of corrosion products on the surface. However, the oxygen content on the CS1018 sample is much larger than that on the aluminum alloy. In addition, there was an observed higher concentration of chlorides on the CS1018 sample. The formation of an

oxide layer on the CS1018 surface and accumulation of chlorides reinforces that it behaved as the anode in the galvanic couple.

Discussion/Analysis

With increasing rotational speed, all of the investigated materials demonstrated an increasing trend of i_{corr}. There was also an increase in the i_{corr} of all materials in 0.6M NaCl from 0.06M NaCl. The E_{corr} of the materials did not provide an identifiable trend at different rotational speeds. Increasing the rotational speed of the sample will reduce the thickness of the diffusive layer at the interface of the material and electrolyte. This diffusive layer thickness reduction, along with the introduction of more oxygen as a result of the non-stagnant solution, will increase the corrosion current density of the investigated materials.

The ZRA tests proved to that were was a small magnitude galvanic current between the coupling of the CS1018 with AA6111 and CS1018 with AA6022. The average measured currents in 0.6M NaCl were 6.79 $\mu A/cm^2$ and 2.82 $\mu A/cm^2$ for CS1018 with AA6111 and CS1018 with AA6022, respectively. The average measured currents in 0.06M NaCl were 0.354 $\mu A/cm^2$ and 0.018 $\mu A/cm^2$ for CS1018 with AA6111 and CS1018 with AA6022, respectively. This is indicative of galvanic coupling in both coupled materials, even though the magnitudes are relatively small.

The EIS experiments in this project did not provide any discernable trends to provide a basis to relate the effect of the rotational speed to the effect on the polarization resistance. The experimentation did provide adequate data to provide a fitting, assuming a Randles' circuit, and did demonstrate a single time constant. Additional experimentation must be repeated for more accurate EIS conclusions. However, with increasing rotational speeds, no observable trends were identified. AA6022 appeared to perform the best in both electrolyte solutions of 0.6M NaCl and 0.06M NaCl. Both AA6022 and CS1018 performed better than AA6111 in 0.06M NaCl.

SKP scans of the samples provided an electrical mapping of the potential gradient that was resultant from the galvanic coupling. After exposure for 5 hours in the solution, the potential scan of the surface demonstrated a

more electropositive potential on the CS1018 in both couples. The AA6111 and AA6022 in both scans demonstrated no significant difference in electrical potentials between the initial scan and 5-hour scan.

Optical Microscopy and SEM demonstrated a clear observation that the CS1018 developed a higher concentration of oxides nearest to the interface between the CS1018 and AA6111 or CS1018 and AA6022. Higher concentrations of oxygen were observed on the CS1018 sample via EDX. AA6111 and AA6022 did not demonstrate an increased formation of oxide or high concentrations of oxygen at the interface.

Overall, the corrosion behavior of AA6022 demonstrated to perform better than the AA6111 in both solutions. It demonstrated lower corrosion current density and more negative corrosion potential. The measured corrosion potential was close to that of the CS1018 in both solutions respectively. This will demonstrate there is a smaller magnitude galvanic coupling effect of AA6022 when coupled with CS1018 in comparison with the AA6111 coupled with CS1018.

Future work involving this project would include building a model of the galvanic couples of each individual aluminum alloy with carbon steel in COMSO: Multiphysics. This would provide an excellent demonstration of the corrosion process and effect of each material, which would predict such behavior accordingly. These modelling tools will provide the automotive industry the tools needed to mitigate this behavior.

Design Analysis

The use of materials that do not accelerate corrosion when coupled together is necessary in order to design better performing systems. Without this knowledge, the lifetime expectancy of the systems that employ these coupled materials will drastically be reduced. With a reduction in lifetime expectancy will come an increase in replacement costs, reduction in safety, and possibly lead to lawsuits from damages that would arise from incidents. A reduction in lifetime will increase the frequency at which remediation efforts must be performed of the galvanic couple. With no remediating efforts being performed, a major safety hazard is present in the system or automotive vehicle. Most remediation measures can be costly to the consumer or manufacturer. In terms of automotive, the

cost of the corrosion and the safety hazard will most likely be passed onto the consumer. With more understanding of the galvanic corrosion effect,

The safety of citizens or other personnel who utilize the systems will also be dramatically increased. By providing an understanding of the galvanic coupling effect and magnitude of these materials, rapid failures that would result will be minimized. This will eliminate any life-threatening and other dangerous harm to personnel that would arise from the coupling of the materials. If no action were to be taken to prevent such incidents, class action lawsuits may occur against a company. This will be highly costly to the company in the short-term in terms of financial assets and in the long-term result in a tarnished reputation that may lead to a loss of revenue.

The financial benefits that would arise from using materials that are not galvanically coupled will be beneficial to the associated company, in addition to reducing the annual cost of corrosion. The annual cost of corrosion in the automotive sector in the United States was reported to be approximately 23.4 billion USD as of 2016. This amount accounted for roughly 7.2% of the automotive GDP in 2016. A reduction in this figure appears to be relatively small in terms of GDP, but it is a sizeable portion when compared with the total annual cost of 254.3 billion USD for the corrosion in the United States. A reduction in the cost of corrosion in the automotive sector will greatly enhance the economic well-being of the country. [20]

The cost of using aluminum alloys is approaching the cost of carbon steel per pound as manufacturing and refining methods of aluminum is improved and becoming more efficient. The cost of aluminum as of 2020 was estimated to be approximately 0.89 USD per pound and is gradually decreasing in cost with time. As of 2010 the average cost of aluminum per pounds was 1.04 USD. The cost of carbon steel as of 2009 was estimated to be between 0.70 and 0.75 USD per pound. The cost of using aluminum alloys is slightly greater than carbon steel, but the reduction in weight is inversely related to the vehicles fuel economy. It has been seen that a weight reduction of 5% resulted in a 2.1% fuel economy increase. [21] [22] [23] [24]

Taking these factors into consideration, a model approach of the galvanic couple can be developed and used in order to provide a statistical assessment of the economic, safety, and technical impact of applying a

galvanic couple into the design of the automotive or other structure. This model will assist in reducing the safety, financial, and economic impact of the corrosion in this sector. The results gained from this model could lead to an eventual standardization of acceptable coupled corrosion rates at specified areas of the two materials used. The modeled rates would be used to provide guidance to any federal departments in regulating the automotive industry to push manufacturers towards safer practices when assessing whether to use galvanically coupled joints. [25]

Acknowledgements

I would like to give the greatest of thanks to both my advisors for this project, Juan Bosch and Dr. David M. Bastidas. They both have provided copious support and feedback during this project and with their dedication this project succeeded. The learning opportunities provided to me from them have been extremely valuable.

In addition, I would like to also thank the University of Akron and NCERCAMP for providing the tools needed to complete this project.

References

[1] Fridlyander, I. N., et al, "Aluminum Alloys: Promising Materials in the Automotive Industry". Metal Science and Heat Treatment, Vol. 44, September 10, 2002

[2] Jones, Denny A. Principles and Prevention of Corrosion. 2nd ed., Prentice-Hall, 1996

[3] Musfirah, A.H., Jaharah A.G., "Magnesium and Aluminum Alloys in Automotive Industry". Journal of Applied Sciences Research, 2012

[4] K.A. Harries. (2014). Enhancing the stability of structural steel components using fibre-reinforced polymer composites. *ScienceDirect.* doi: 10.1533

[5] McCafferty, E. Introduction to Corrosion Science. Springer, 2010

[6] Mansfeld, F., Kenkel, J.V., "Galvanic Corrosion of Al Alloys – III. The effect of area ratio". Corrosion Science, Vol. 15, 1975.

[7] Esmailzadeh, Samaneh & Aliofkhazraei, Mahmood & Sarlak, Hossein. (2018). interpretation of cyclic potentiodynamic polarization test results for study of corrosion behavior of metals: A Review. Protection of Metals and Physical Chemistry of Surfaces. 54. 976-989. 10.1134/S207020511805026X

[8] Habib, K., “Zero resistance ammeter of metallic alloys in aqueous solutions”. Optik, Vol. 118, 2007

[9] ASTM G71-81, “Standard guide for conducting and evaluating galvanic corrosion tests in electrolytes”. ASTM International. West Conshohocken, PA, USA, 2019. doi: 2018

[10] Ciucci, F., “Modeling Electrochemical Impedance Spectroscopy”. Current Opinon in Electrochemistry, 2019

[11] Juttner, K., “Electrochemical impedance spectroscopy (EIS) of corrosion processes in inhomogeneous surfaces”. Electrochimica Acta, Vol. 25, 1990

[12] ASTM G106-89 “Standard practice for verification of algorithm and equipment for electrochemical impedance measurements”. ASTM International. West Conshohocken, PA, USA, 2019. doi: 2015

[13] Arabzadeh H, Shahidi M, Foroughi MM. (2017). Electrodeposited polypyrrole coatings on mild steel: modeling the EIS data with a new equivalent circuit and the influence of scan rate and cycle number on the corrosion protection. Journal of Electroanalytical Chemistry 807(1): 162-173.

[14] Walsh, F.C., et al, “The rotating cylinder electrode for studies of corrosion engineering and protection of metals – an illustrated review”. Corrosion Science, 2017

[15] Rohwerder, M., Turcu, F., “High-resolution Kelvin probe microscopy in corrosion Science: Scanning Kelvin probe forced microscopy (SKPFM) versus classical scanning Kelvin probe (SKP)”. Electrochimica Acta, 2007

[16] Jonsson, M., et al, “The influence of microstructure on the corriosion behaviour of AZ91D studied by scanning Kelvin probe forcé microscopy and scanning Kelvin probe”. Corrosion Science, Vol. 48, 2006

[17] Charrier, D.S.H., et al, “Real versus measured surface potentials in scanning Kelvin probe microscopy”. ACS Nano, Vol. 2, 2008

[18] Grimnes, S., Martinsen, O.G., “Bioimpedance and Bioelectricity Basics”. 2015

[19] ASTM G31 “Standard guide for laboratory immersion corrosion testing of metals”. ASTM International. West Conshohocken, PA, USA, 2019. doi: 2021

[20] Koch, G., et al, “International Measures of Prevention, Application, and Economics of Corrosion Technologies Study”. NACE International, 2016.

[21] Garside, M. “U.S. Aluminum Market Price 2010-2020.” Statista, 11 Feb. 2021, www.statista.com/statistics /209336/price-of-aluminum-on-the-us-market/#:~:text=In%202020%2C%20the%20average%20market, 89%20U.S.%20cents%20per%20pound.

[22] Scott, E. “ASA Materials Market Digest”. American Supply Association, 2009.

[23] Joost, W.J., “Reducing Vehicle Weight and Improving U.S. Energy Efficiency Using Integrated Computational Materials Engineering”. U.S. Department of Energy, 2012.

[24] “Save Money and Fuel by Driving Efficiently.” Www.fueleconomy.gov - the Official Government Source for Fuel Economy Information, www.fueleconomy.gov/feg/driveHabits.jsp.

[25] Melchers, R.E., “Predicting long-term corrosion of metal alloys in physical infrastructure”. Materials Degradation, 2018.

Addendum

Aluminum alloys are a steadily growing material being commonly used in lieu of typical steels because of their low weight and high strength. Additional alloying, heat treatment, and other property enhancing processes are expanding the use of these alloys. However, with this expansion, galvanic corrosion is becoming more of an issue in design due to the combination of these alloys with steels.

Additional understanding is required on the mechanism and kinetics of this issue in order to better mitigate and design the systems that employ these alloys. For this study, three materials were investigated individually and coupled in two solutions. The materials were carbon steel 1018, aluminum alloys 6111 and 6022. The investigated solutions were 0.6M NaCl and 0.06M NaCl. To simulate the effects of atmospheric environments, rotating disk electrode setup was used while performing cyclic potentiodynamic polarization and electrochemical impedance spectroscopy. The investigated speeds were 0, 100, 500, 1000, and 2000 rpm. Scanning Kelvin Probe was performed to characterize the potential gradient resultant from the galvanic coupling. The measured galvanic current between the carbon steel and both aluminum alloys were indicative of galvanic coupling in both solutions.